

Strong electron-phonon coupling and phonon-induced superconductivity in tetragonal C_3N_4 with hole doping

Alexander N. Rudenko,^{1,*} Danis I. Badrtdinov,¹ Igor A. Abrikosov,² and Mikhail I. Katsnelson¹

¹*Radboud University, Institute for Molecules and Materials, Heijendaalseweg 135, 6525AJ Nijmegen, The Netherlands*

²*Department of Physics, Chemistry, and Biology (IFM), Linköping University, SE-581 83, Linköping, Sweden*

(Dated: September 1, 2023)

C_3N_4 is a recently discovered phase of carbon-nitrides with the tetragonal crystal structure (arXiv:2209.01968) that is stable at ambient conditions. C_3N_4 is a semiconductor exhibiting flat-band anomalies in the valence band, suggesting the emergence of many-body instabilities upon hole doping. Here, using state-of-the-art first-principles calculations we show that hole-doped C_3N_4 reveals strong electron-phonon coupling, leading to the formation of a gapped superconducting state. The phase transition temperatures turn out to be strongly dependent on the hole concentration. We propose that holes could be injected into C_3N_4 via boron doping which induces, according to our results, a rigid shift of the Fermi energy without significant modification of the electronic structure. Based on the electron-phonon coupling and Coulomb pseudopotential calculated from first principles, we conclude that the boron concentration of 6 atoms per nm^3 would be required to reach the critical temperature of ~ 55 K at ambient pressure.

The prospects of high-temperature superconductivity attract enormous attention to this phenomenon [1–3]. In this respect, the performance of conventional superconductors, i.e. those mediated by the electron-phonon pairing mechanism, are believed to be limited. Nevertheless, there has been a considerable progress in the experimental discovery of phonon-mediated superconductivity in hydrides with reported critical temperatures T_c of up to 260 K at extremely high pressures (above 100 GPa) [4–8]. A promising direction in attaining high T_c is to focus on compounds with light elements that permit the existence of high-frequency phonons strongly coupled to charge carriers. This strategy was suggested by Ashcroft [9] as a practical realization of his old idea of superconductivity of metallic hydrogen [10]. From this perspective, the role of heavy elements is just to provide a container for solid hydrogen, assuming that the hydrogen contribution to the electron states at the Fermi level is essential.

Other light elements are obvious candidates for obtaining superconductors with reasonably high T_c . MgB_2 with $T_c \approx 40$ K is probably the most known example [11, 12]. As for the next to boron element in the Periodic Table, carbon, intercalated graphite and graphene laminates were also intensively studied both experimentally [13–15] and theoretically [16–19] but the reached T_c 's are always essentially smaller than for MgB_2 . Here, we predict theoretically the phonon-mediated superconductivity in another group of light-element compounds, namely, carbon nitrides, with one of the highest critical temperatures than in any other currently known conventional superconductors at ambient pressure.

A number of previously unknown crystalline phases of nitrogen and its compounds have been discovered in the past years by means of high-pressure synthesis [20–22]. Recently, the synthesis of ultra-incompressible carbon nitrides recoverable at ambient conditions has been

reported [23]. Among them, a tetragonal phase C_3N_4 with the space group $I\bar{4}2m$ demonstrates remarkable electronic properties. Particularly, C_3N_4 is a semiconductor with the flat-band features near the top of the valence band, suggesting essential role of many-body effects upon hole doping. In combination with high-frequency (~ 160 meV) phonons, such characteristics make C_3N_4 an appealing candidate for superconductivity, which constitutes the main focus of our study.

Computational details — First-principles electronic structure and total energy calculations were performed using density functional theory (DFT) within the plane-wave pseudopotential method [24] as implemented in the QUANTUM ESPRESSO distribution [25, 26]. The exchange-correlation effects were considered within the generalized-gradient approximation (GGA) functional in the Perdew-Burke-Ernzerhof parametrization [27]. Ultrasoft pseudopotentials were used with a 50 Ry energy cutoff for the plane waves and 400 Ry for the charge density [28]. The lattice dynamics and phonon-related properties were calculated within the density-functional perturbation theory (DFPT) [29]. To achieve convergence in the calculation of the superconducting properties, the electron-phonon interactions were interpolated using the Wannier functions [30, 31] as implemented in the EPW package [32]. The Wannier functions were constructed from the manifold of four valence states using the procedure of maximum localization [33, 34], resulting in one p -like orbital per N atom. The Brillouin zone was sampled by $(12 \times 12 \times 12)$ \mathbf{k} -point and $(6 \times 6 \times 6)$ \mathbf{q} -point meshes in the DFT and DFPT calculations, respectively. The Brillouin zone integrals were calculated using interpolated \mathbf{k} - and \mathbf{q} -meshes. The numerical integration was performed using the Gaussian smearing with the parameters 10 and 0.5 meV for electrons and phonons, respectively. Convergence tests of the BZ integrals are provided in SM [35].

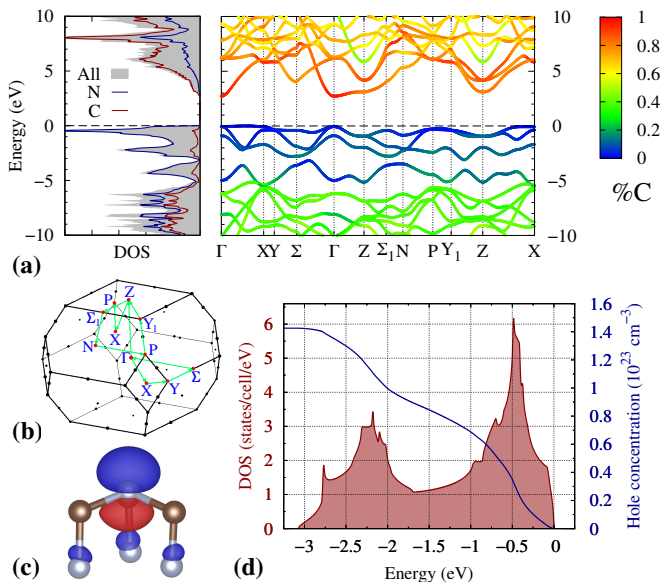


FIG. 1. (a) DOS and band structure projected onto the sp states of N and C atoms in C_3N_4 . Color indicates the contribution of N (blue) or C (red) states. The Brillouin zone (BZ) of the tetragonal lattice of C_3N_4 with the high-symmetry directions along which the band structure is calculated. (c) p_z -like Wannier orbital residing on N atoms describing the valence states in C_3N_4 . (d) DOS of the valence band (shaded area) and the hole concentration (blue solid line) shown as a function of energy. Zero energy corresponds to the valence band top.

Dielectric screening and the Coulomb interactions in undoped C_3N_4 were calculated in the Wannier basis using the random phase approximation (RPA) as implemented in VASP [36–38]. To this end, we carried out calculations within the projector augmented wave formalism (PAW) [39] using GGA and a 400 eV cutoff for the plane waves. The polarization function was calculated taking a window of ~ 100 eV for the empty states. The calculation of the Coulomb interactions and screening in doped C_3N_4 was performed using an in-house developed code.

Electronic structure — Figure 1(a) shows the band structure and density of states (DOS) calculated for C_3N_4 along the high-symmetry directions of the Brillouin zone shown in Fig. 1(b). From Fig. 1(a) one can see that the valence band is predominantly formed by the sp states of N atoms, while C atoms mainly contribute to the conduction band. The valence N states are well isolated within the range from -5 to 0 eV. The subspace of N valence states can be represented in terms of equivalent p_z -like Wannier orbitals, each centered on N atoms, as visualized in Fig. 1(c). The GGA electronic structure of C_3N_4 exhibits an indirect band gap of ~ 2.7 eV. The conduction band bottom is located at the Γ point, whereas the valence band top is in-between the Γ and X points, forming a saddle point at the Γ point ~ 0.06 eV below the valence band top. This saddle point gives

rise to a van Hove singularity which, however, does not form an isolated peak in DOS. At the same time, there is another vHS close to the valence band top at ~ -0.5 eV, originating from the flat band along the Y - Σ direction, giving rise to a prominent peak in DOS. The proximity of vHS to the valence band edge suggests that the system could be potentially p -doped in order to align the vHS with the Fermi energy. This, in turn, might lead to the emergence of many-body effects and exotic physics. Practically, hole doping in C_3N_4 could be achieved by the doping of B atoms, which tend to replace C atoms, which is discussed below. The dependence of the hole concentration on the Fermi energy is shown in Fig. 1(d).

Phonons and electron-phonon coupling — Figure 2(a) shows the phonon dispersion $\omega_{\mathbf{q}\nu}$ along with the phonon linewidths $\gamma_{\mathbf{q}\nu} \sim N_F \lambda_{\mathbf{q}\nu} \omega_{\mathbf{q}\nu}^2$ calculated at $T = 50$ K and $E_F = -25$ meV. The phonon spectrum exhibits three linearly-dispersing branches in the range up to ~ 50 meV and a bunch of optical branches extending up to ~ 160 meV, similar to diamond [40]. The high-frequency character of optical phonons in C_3N_4 is determined by the low atomic masses and strong interatomic bonding. Overall, the spectrum is typical for a 3D compound, showing no anomalies. At high frequencies, there is an apparent broadening of the phonon lines, i.e. along the Σ - Γ and Γ - Z directions, indicating strong electron-phonon interaction at specific wave vectors \mathbf{q} . This gives rise to a sharp high-energy peak in the Eliashberg function

$$\alpha^2 F(\omega) = \frac{1}{2} \sum_{\mathbf{q}\nu} \omega_{\mathbf{q}\nu} \lambda_{\mathbf{q}\nu} \delta(\omega - \omega_{\mathbf{q}\nu}), \quad (1)$$

shown in Fig. 2(b) for three different E_F , from which one can see that the dominant contribution to the electron-phonon coupling originates from the high-energy region. In Eq. (1), $\lambda_{\mathbf{q}\nu} = \langle |g_{\mathbf{q}\nu}^{\nu}|^2 \rangle / \omega_{\mathbf{q}\nu}$ is the momentum resolved electron-phonon coupling constant averaged over the Fermi surface with

$$g_{\mathbf{k}\mathbf{k}'}^{nn',\nu} = \sqrt{\frac{\hbar}{2m_0\omega_{\mathbf{q}\nu}}} \langle \psi_{n'\mathbf{k}'} | \partial_{-\mathbf{q}\nu} V | \psi_{n\mathbf{k}} \rangle \quad (2)$$

being the matrix element of the electron-phonon interaction, where $\partial_{-\mathbf{q}\nu} V$ is the phonon-induced variation of the electronic potential written in the basis of Bloch states $\psi_{n\mathbf{k}}$. Figure 2(c) shows the integrated electron-phonon coupling $\lambda = 2 \int d\omega \frac{\alpha^2 F(\omega)}{\omega}$ as a function of E_F . Already at $E_F = -50$ meV, we obtain $\lambda = 0.6$, which can be qualified as a strong regime [41]. The energy-dependence of λ closely follows electronic DOS, indicating that the strong coupling in C_3N_4 is governed by the peculiarities of its electronic structure.

At the same time, in the absence of magnetism, large λ suggests an instability with respect to the formation of a superconducting state. Ignoring the Coulomb interaction, a simple estimate using the Allen-Dynes formula

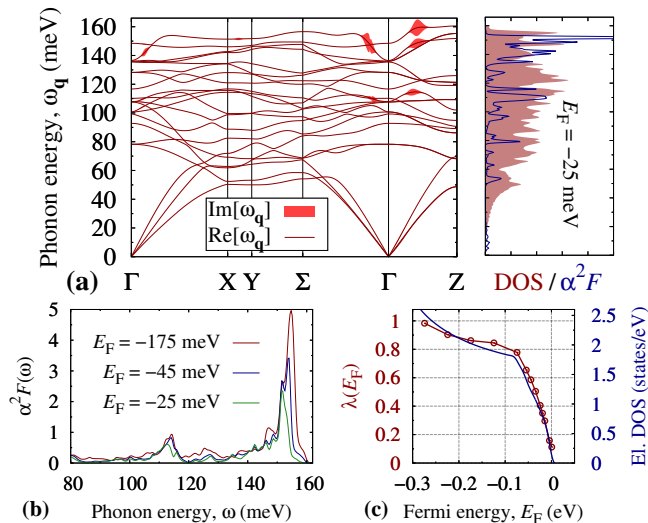


FIG. 2. (a) Phonon dispersion (lines) and the corresponding linewidths (filled areas) calculated for the Fermi energy $E_F = -25$ meV and $T = 50$ K along selected high-symmetry directions of the Brillouin zone in C_3N_4 . Right panel shows phonon DOS (shaded area) and the Eliashberg function $\alpha^2 F(\omega)$ (blue solid line) calculated for $E_F = -25$ meV. (b) High-frequency region of $\alpha^2 F(\omega)$ plotted for three different E_F . (c) Electron phonon constant λ shown as a function of the Fermi energy E_F superimposed onto the electron DOS.

[42] yields $T_c = 68$ K for $E_F = -50$ meV. In what follows, we analyze the possibility for conventional superconductivity in C_3N_4 in more detail.

Coulomb interaction — Before we proceed to a more rigorous analysis of the superconductivity in C_3N_4 , we consider the problem of the electron-electron repulsion, which is another crucial factor for conventional superconductivity.

Electron-electron interaction constant averaged over the Fermi surface can be written as

$$\mu_C = N_F^{-1} \sum_{mn} \sum_{\mathbf{k}\mathbf{k}'} W_{\mathbf{k}-\mathbf{k}'} \delta(E_{n\mathbf{k}} - E_F) \delta(E_{m\mathbf{k}'} - E_F), \quad (3)$$

where $N_F = \sum_{n\mathbf{k}} \delta(E_{n\mathbf{k}} - E_F)$ is DOS at the Fermi energy. To estimate the Coulomb interaction, we employ the random phase approximation (RPA) [43, 44], in which $W_{\mathbf{q}} = V_{\mathbf{q}}(1 - \Pi_{\mathbf{q}}V_{\mathbf{q}})^{-1}$ with $V_{\mathbf{q}}$ being the bare (unscreened) interaction, and $\Pi_{\mathbf{q}}$ being the static polarizability. We first consider the Coulomb interaction in C_3N_4 without doping. To this end, we calculate the bare $V(r_{ij}) = \langle \phi_i \phi_i | r_{ij}^{-1} | \phi_j \phi_j \rangle$ and screened $U(r_{ij})$ Coulomb interaction between the relevant N- p_z orbitals as a function of the interorbital distance r_{ij} , shown in Fig. 3(a). The screened interaction is calculated within (RPA) $U_{\mathbf{q}} = V_{\mathbf{q}} + V_{\mathbf{q}}\Pi_{\mathbf{q}}^{(0)}U_{\mathbf{q}}$ with $\Pi_{\mathbf{q}}^{(0)}$ being the static polarizability of undoped C_3N_4 . Due to sufficient localization of the N orbitals, the bare interaction fits very well to the classical $V(r) = e^2/r$ law except the point $r = 0$, which is irrelevant for the purpose of our study.

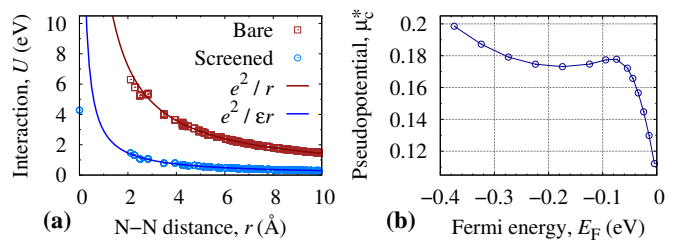


FIG. 3. (a) Bare and screened Coulomb interaction calculated between the relevant p_z -like orbitals of N in C_3N_4 as a function of the interorbital distance r . Lines are obtained by fitting to the classical Coulomb law. (b) Coulomb pseudopotential μ_C^* shown as a function of the Fermi energy E_F .

To a good approximation, the screened interaction $U(r)$ can be obtained by the rescaling $V(r) \rightarrow V(r)/\epsilon$, which allows us to determine the dielectric constant in undoped C_3N_4 , which is found to be $\epsilon = 4.9$. Upon the doping, there is another (metallic) contribution to the screening, which is essentially \mathbf{q} - and doping-dependent. In order to take this contribution into account, we calculate the metallic contribution to the polarizability $\Pi_{\mathbf{q}}^{(1)}$ considering the N valence states separately, within the model discussed earlier. The resulting Coulomb interaction can be then written as $W_{\mathbf{q}} = U_{\mathbf{q}}(1 - \Pi_{\mathbf{q}}^{(1)}U_{\mathbf{q}})^{-1}$, where $U_{\mathbf{q}} = 4\pi e^2/\epsilon q^2$.

In the Eliashberg theory of superconductivity [45] it is a common practice to deal with the logarithmically-corrected Coulomb interaction, giving rise to the well-known pseudopotential [46, 47]

$$\mu_C^* = \frac{\mu_C}{1 + \mu_C \ln(\omega_{el}/\omega_{ph})}. \quad (4)$$

Here, ω_{el} and ω_{ph} are the energy cutoffs for electrons and phonons, which characterize decay of the interactions away from the Fermi surface. The phonon cutoff is determined by the highest Matsubara frequency used to solve the Eliashberg equations. In our case, we set $\omega_{ph} = 5\omega_{ph}^{\max} \approx 0.8$ eV. The characteristic energy of the Coulomb interactions is related to the decay of single-particle excitations, and can be associated with the energy of plasma excitations, $\omega_{el} \simeq \omega_{p1}$. In C_3N_4 , the lowest plasma resonance, determined from the condition $\text{Re}[\epsilon_{\mathbf{q}=0}(\omega_{p1})] = 0$, corresponds to $\omega_{p1} \approx 13.9$ eV [35]. The resulting μ_C^* is shown in Fig. 3(b), demonstrating a variation between 0.1 and 0.2, depending on the Fermi energy.

Superconductivity — We now determine temperature-dependence of the superconducting gap $\Delta_0(T)$ as well as its dependence of the Fermi energy in C_3N_4 . To this end, we solve the isotropic Eliashberg equations [45] on the imaginary axis [35] using the coupling parameters obtained earlier. Figure 4(a) shows the calculated critical temperature in C_3N_4 as a function of the Fermi energy. The results are shown for the calculated μ_C^* pre-

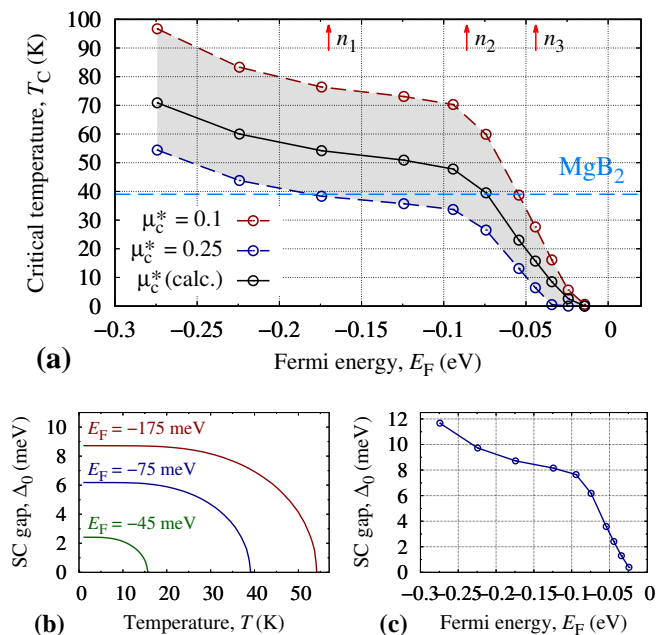


FIG. 4. (a) Critical temperature obtained from solving the isotropic Eliashberg equations for C_3N_4 for different E_F . The results for the Coulomb potentials $\mu_C^* = 0.1$ and 0.25 are shown for reference. Red arrows indicate the Fermi energies that are achievable through the doping by boron with the concentrations $n = 6, 3,$ and 2 B atoms per nm^3 . (b) Energy gap of the superconducting state Δ_0 as a function of temperature for three different E_F . (c) Δ_0 calculated at $T = 0$ K as a function of E_F . Horizontal blue line shows T_c of MgB_2 given for reference.

sented in Fig. 3(b), as well as for the two reference values $\mu_C^* = 0.1$ and 0.25 , representing boundaries of the typical Coulomb pseudopotential. The dependence T_c vs. E_F resembles electronic DOS with a steep increase up to -0.1 eV followed by a moderate growth. Already at $E_F = -0.05$ meV the estimated $T_c \approx 20$ K, increasing up to 65 K at $E_F = -0.25$ eV. The obtained critical temperatures are weakly susceptible to the specific μ_C^* values. Fig. 4(b) displays a typical temperature-dependence of the superconducting gap Δ_0 for three representative Fermi energies. Fig. 4(c) shows $\Delta_0(T = 0)$ for a given Fermi energy. The gap opens up at $E_F = -15$ meV, which corresponds to a hole concentration of $\sim 2 \times 10^{20} \text{ cm}^{-3}$. At zero temperature and small dopings, we obtain the ratio $2\Delta_0/T_c \approx 3.5$, which is close to the BCS result for the weak coupling regime (3.53). At higher dopings, this ratio increases up to 3.8 at $E_F = -0.27$ eV, which lies in-between the weak (3.53) and strong (3.4) coupling regimes in BCS theory [48].

Discussion — The predicted critical temperatures in doped C_3N_4 are fairly large for conventional superconductivity, and may even reach liquid nitrogen temperature at high enough doping. Up to now, we did not specify how the hole doping could be realized in C_3N_4 . In

analogy to diamond [49, 50], where boron demonstrate the ability to substitute carbon atoms and induce hole doping without significant changes in the electronic structure, we propose a similar mechanism for C_3N_4 .

Unlike diamond, there are two possibilities for the substitutional doping in C_3N_4 , where dopants may replace C or N atoms. In order to check whether this process is energetically favorable, we calculated the formation energy of a boron dopant in C_3N_4 , considering the replacement of C and N atoms individually [35]. We find that the substitution of C atoms by boron is considerably more favorable with the formation energies lying between -2.4 and -0.6 eV depending on dopant concentration and the formation conditions. On the contrary, the formation energy of the N substitution is in-between -0.5 and $+0.6$ eV, demonstrating that this type of B-doping is considerably less likely.

We now analyze the electronic structure of C_3N_4 doped by B atoms substituting C atoms. To this end, we consider three different supercells with one B atom per cell, corresponding to the concentration of $6, 3,$ and 2 B atoms per nm^3 . The calculated electronic DOS presented in Fig. S2 [35] shows that the presence of boron defect does not induce any midgap states, but leads to a shift of the Fermi energy into the valence band, indicating p -type doping. The shift of the Fermi energy increases with the B concentration. This demonstrates that the rigid shift model of the hole doping in C_3N_4 is well justified up to the boron concentrations of $6 \times \text{B} / \text{nm}^3$, which allows to achieve the hole density of $\sim 10^{22} \text{ cm}^{-3}$. Under these conditions, the superconducting critical temperature is estimated to be around 55 K (Fig. 4). At higher B dopings, a more significant modification of the electronic structure is expected, limiting the applicability of the rigid band-shift approximation.

Lastly, we comment on the dynamical stability of C_3N_4 in the presence of hole doping. The presence of van Hove singularities and related anomalies in the electronic spectrum often causes softening of the phonon modes, developing dynamical instabilities of the atomic structures [51, 52]. In order to rule out this scenario for C_3N_4 , we calculate the phonon dispersion under the hole doping induced by adding a positive charge to the system. Our calculations presented in Fig. S3 [35] demonstrate the absence of imaginary phonon modes in C_3N_4 up to the concentrations of at least $0.4 \times 10^{23} \text{ cm}^{-3}$, which suggests that the system remains dynamically stable in the relevant range of hole concentrations.

Conclusion — Summarizing, we performed a systematic study of the electron-phonon interaction and superconductivity in a recently discovered tetragonal phase of the carbon nitride C_3N_4 . C_3N_4 features flat-band anomalies in the electronic spectrum, suggesting the development of many-body instabilities upon hole doping. Using state-of-the-art first-principles calculations, we demonstrated that hole-doped C_3N_4 exhibits strong

electron-phonon coupling with the constant $\lambda \lesssim 1$, originating mainly from the high-frequency part (~ 150 meV) of the phonon spectrum. In turn, large λ permits the emergence of conventional superconductivity even at moderate dopings. The critical temperature of the superconducting transition is estimated from solving the Eliashberg equations on the imaginary axis. For this purpose, we carefully estimated the Coulomb pseudopotential μ_C^* , which turns out to be doping-dependent, lying between 0.1–0.2 for the relevant doping regime. Our calculations show that T_c steadily increase with the hole concentration, reaching $T_c \simeq 55$ K at $n_h \simeq 1 \times 10^{22}$ cm $^{-3}$. We demonstrate that this concentration could be achieved by doping C₃N₄ with boron. At moderate concentrations up to $6 \times B / \text{nm}^3$, the electronic structure of C₃N₄ remains essentially unchanged with the exception of the Fermi energy shift, manifesting itself a *p*-type doping. At the same time, we do not exclude that even higher doping levels, i.e. higher T_c , could be reached by other dopants.

Our findings expand the spectrum of ambient-pressure conventional superconductors with relatively high T_c , and call for its experimental verification. We note that the presence of flat bands in C₃N₄ might trigger other many-body instabilities even at higher temperatures, potentially leading to the formation of different exotic states of matter such as charge density waves or *sp* magnetism. This paves the way for further research in this direction. Finally, it is worth mentioning that multiple other phases of the recently discovered carbon nitrides [23] with ultraincompressibility also represent a promising playground for further superconductivity studies.

The work was supported by European Research Council via Synergy Grant 854843 - FASTCORR. IAA is Wallenberg Scholar (grant no. KAW-2018.0194). IAA acknowledges support provided by the Swedish Research Council (VR) Grant No. 2019-05600 and by the Swedish Government Strategic Research Area in Materials Science on Functional Materials at Linköping University (Faculty Grant SFO-Mat-LiU No. 2009 00971).

* a.rudenko@science.ru.nl

- [1] J. A. Flores-Livas, L. Boeri, A. Sanna, G. Profeta, R. Arita, and M. Eremets, A perspective on conventional high-temperature superconductors at high pressure: Methods and materials, *Phys. Rep.* **856**, 1 (2020), a perspective on conventional high-temperature superconductors at high pressure: Methods and materials.
- [2] B. Lilia, R. Hennig, P. Hirschfeld, G. Profeta, A. Sanna, E. Zurek, W. E. Pickett, M. Amsler, R. Dias, M. I. Eremets, C. Heil, R. J. Hemley, H. Liu, Y. Ma, C. Pierleoni, A. N. Kolmogorov, N. Rybin, D. Novoselov, V. Anisimov, A. R. Oganov, C. J. Pickard, T. Bi, R. Arita, I. Errea, C. Pellegrini, R. Requist, E. K. U. Gross, E. R. Margine, S. R. Xie, Y. Quan, A. Hire, L. Fanfarillo, G. R. Stewart, J. J. Hamlin, V. Stanev, R. S. Gonnelli, E. Piatti, D. Romanin, D. Daghero, and R. Valenti, The 2021 room-temperature superconductivity roadmap, *J. Phys.: Condens. Matter* **34**, 183002 (2022).
- [3] W. E. Pickett, Colloquium: Room temperature superconductivity: The roles of theory and materials design, *Rev. Mod. Phys.* **95**, 021001 (2023).
- [4] A. P. Drozdov, M. I. Eremets, I. A. Troyan, V. Ksenofontov, and S. I. Shylin, Conventional superconductivity at 203 kelvin at high pressures in the sulfur hydride system, *Nature* **525**, 73 (2015).
- [5] M. Somayazulu, M. Ahart, A. K. Mishra, Z. M. Geballe, M. Baldini, Y. Meng, V. V. Struzhkin, and R. J. Hemley, Evidence for Superconductivity above 260 K in Lanthanum Superhydride at Megabar Pressures, *Phys. Rev. Lett.* **122**, 027001 (2019).
- [6] A. P. Drozdov, P. P. Kong, V. S. Minkov, S. P. Besedin, M. A. Kuzovnikov, S. Mozaffari, L. Balicas, F. F. Balakirev, D. E. Graf, V. B. Prakapenka, E. Greenberg, D. A. Knyazev, M. Tkacz, and M. I. Eremets, Superconductivity at 250 K in lanthanum hydride under high pressures, *Nature* **569**, 528 (2019).
- [7] E. Snider, N. Dasenbrock-Gammon, R. McBride, X. Wang, N. Meyers, K. V. Lawler, E. Zurek, A. Salamat, and R. P. Dias, Synthesis of yttrium superhydride superconductor with a transition temperature up to 262 k by catalytic hydrogenation at high pressures, *Phys. Rev. Lett.* **126**, 117003 (2021).
- [8] P. Kong, V. S. Minkov, M. A. Kuzovnikov, A. P. Drozdov, S. P. Besedin, S. Mozaffari, L. Balicas, F. F. Balakirev, V. B. Prakapenka, S. Chariton, D. A. Knyazev, E. Greenberg, and M. I. Eremets, Superconductivity up to 243 K in the yttrium-hydrogen system under high pressure, *Nat. Commun.* **12**, 5075 (2021).
- [9] N. W. Ashcroft, Hydrogen dominant metallic alloys: High temperature superconductors?, *Phys. Rev. Lett.* **92**, 187002 (2004).
- [10] N. W. Ashcroft, Metallic hydrogen: A high-temperature superconductor?, *Phys. Rev. Lett.* **21**, 1748 (1968).
- [11] J. Nagamatsu, N. Nakagawa, T. Muranaka, Y. Zenitani, and J. Akimitsu, Superconductivity at 39 K in magnesium diboride, *Nature* **410**, 63 (2001).
- [12] A. Y. Liu, I. I. Mazin, and J. Kortus, Beyond Eliashberg Superconductivity in MgB₂: Anharmonicity, Two-Phonon Scattering, and Multiple Gaps, *Phys. Rev. Lett.* **87**, 087005 (2001).
- [13] T. E. Weller, M. Ellerby, S. S. Saxena, R. P. Smith, and N. T. Skipper, Superconductivity in the intercalated graphite compounds C₆Yb and C₆Ca, *Nat. Phys.* **1**, 39 (2005).
- [14] S. Heguri, N. Kawade, T. Fujisawa, A. Yamaguchi, A. Sumiyama, K. Tanigaki, and M. Kobayashi, Superconductivity in the graphite intercalation compound *ba*c₆, *Phys. Rev. Lett.* **114**, 247201 (2015).
- [15] J. Chapman, Y. Su, C. A. Howard, D. Kundys, A. N. Grigorenko, F. Guinea, A. K. Geim, I. V. Grigorieva, and R. R. Nair, Superconductivity in ca-doped graphene laminates, *Sci. Rep.* **6**, 23254 (2016).
- [16] G. Profeta, M. Calandra, and F. Mauri, Phonon-mediated superconductivity in graphene by lithium deposition, *Nat. Phys.* **8**, 131 (2012).
- [17] E. R. Margine and F. Giustino, Two-gap superconductivity in heavily *n*-doped graphene: Ab initio migdal-

- eliashberg theory, *Phys. Rev. B* **90**, 014518 (2014).
- [18] E. R. Margine, H. Lambert, and F. Giustino, Electron-phonon interaction and pairing mechanism in superconducting ca-intercalated bilayer graphene, *Sci. Rep.* **6**, 21414 (2016).
- [19] J.-J. Zheng and E. R. Margine, First-principles calculations of the superconducting properties in li-decorated monolayer graphene within the anisotropic migdal-eliashberg formalism, *Phys. Rev. B* **94**, 064509 (2016).
- [20] M. I. Eremets, A. G. Gavriliuk, I. A. Trojan, D. A. Dzivenko, and R. Boehler, Single-bonded cubic form of nitrogen, *Nat. Mater.* **3**, 558 (2004).
- [21] D. Laniel, B. Winkler, T. Fedotenko, A. Pakhomova, S. Chariton, V. Milman, V. Prakapenka, L. Dubrovinsky, and N. Dubrovinskaia, High-Pressure Polymeric Nitrogen Allotrope with the Black Phosphorus Structure, *Phys. Rev. Lett.* **124**, 216001 (2020).
- [22] M. Bykov, T. Fedotenko, S. Chariton, D. Laniel, K. Glazyrin, M. Hanfland, J. S. Smith, V. B. Prakapenka, M. F. Mahmood, A. F. Goncharov, A. V. Ponomareva, F. Tasnádi, A. I. Abrikosov, T. Bin Masood, I. Hotz, A. N. Rudenko, M. I. Katsnelson, N. Dubrovinskaia, L. Dubrovinsky, and I. A. Abrikosov, High-Pressure Synthesis of Dirac Materials: Layered van der Waals Bonded BeN₄ Polymorph, *Phys. Rev. Lett.* **126**, 175501 (2021).
- [23] D. Laniel, F. Trybel, A. Aslandukov, S. Khandarkhaeva, T. Fedotenko, Y. Yin, F. Tasnádi, A. V. Ponomareva, G. Weck, F. I. Akbar, B. Winkler, A. Néri, S. Chariton, C. Giacobbe, J. Wright, G. Garbarino, B. Wehinger, A. Pakhomova, M. Mezouar, V. Prakapenka, V. Milman, W. Schnick, I. A. Abrikosov, L. Dubrovinsky, and N. Dubrovinskaia, Synthesis of ultra-incompressible carbon nitrides featuring three-dimensional frameworks of cn4 tetrahedra recoverable at ambient conditions (2022), [arXiv:2209.01968 \[cond-mat.mtrl-sci\]](https://arxiv.org/abs/2209.01968).
- [24] D. Vanderbilt, Soft self-consistent pseudopotentials in a generalized eigenvalue formalism, *Phys. Rev. B* **41**, 7892 (1990).
- [25] P. Giannozzi, S. Baroni, N. Bonini, M. Calandra, R. Car, C. Cavazzoni, D. Ceresoli, G. L. Chiarotti, M. Cococcioni, I. Dabo, A. D. Corso, S. de Gironcoli, S. Fabris, G. Fratesi, R. Gebauer, U. Gerstmann, C. Gougoussis, A. Kokalj, M. Lazzeri, L. Martin-Samos, N. Marzari, F. Mauri, R. Mazzarello, S. Paolini, A. Pasquarello, L. Paulatto, C. Sbraccia, S. Scandolo, G. Sclauzero, A. P. Seitsonen, A. Smogunov, P. Umari, and R. M. Wentzcovitch, QUANTUM ESPRESSO: a modular and open-source software project for quantum simulations of materials, *J. Phys.: Condens. Matter* **21**, 395502 (2009).
- [26] P. Giannozzi, O. Andreussi, T. Brumme, O. Bunau, M. B. Nardelli, M. Calandra, R. Car, C. Cavazzoni, D. Ceresoli, M. Cococcioni, N. Colonna, I. Carnimeo, A. D. Corso, S. de Gironcoli, P. Delugas, R. A. DiStasio, A. Ferretti, A. Floris, G. Fratesi, G. Fugallo, R. Gebauer, U. Gerstmann, F. Giustino, T. Gorni, J. Jia, M. Kawamura, H.-Y. Ko, A. Kokalj, E. Küçükbenli, M. Lazzeri, M. Marsili, N. Marzari, F. Mauri, N. L. Nguyen, H.-V. Nguyen, A. O. de-la Roza, L. Paulatto, S. Poncé, D. Rocca, R. Sabatini, B. Santra, M. Schlipf, A. P. Seitsonen, A. Smogunov, I. Timrov, T. Thonhauser, P. Umari, N. Vast, X. Wu, and S. Baroni, Advanced capabilities for materials modelling with Quantum ESPRESSO, *J. Phys.: Condens. Matter* **29**, 465901 (2017).
- [27] J. P. Perdew, K. Burke, and M. Ernzerhof, Generalized Gradient Approximation Made Simple, *Phys. Rev. Lett.* **77**, 3865 (1996).
- [28] We used the pseudopotentials C.pbe-nrrkjus_psl.1.0.0.UPF, N.pbe-nrrkjus_psl.1.0.0.UPF, and B.pbe-nrrkjus_psl.1.0.0.UPF from <http://www.quantum-espresso.org>.
- [29] S. Baroni, S. de Gironcoli, A. Dal Corso, and P. Giannozzi, Phonons and related crystal properties from density-functional perturbation theory, *Rev. Mod. Phys.* **73**, 515 (2001).
- [30] F. Giustino, M. L. Cohen, and S. G. Louie, Electron-phonon interaction using wannier functions, *Phys. Rev. B* **76**, 165108 (2007).
- [31] F. Giustino, Electron-phonon interactions from first principles, *Rev. Mod. Phys.* **89**, 015003 (2017).
- [32] S. Poncé, E. Margine, C. Verdi, and F. Giustino, Epw: Electron-phonon coupling, transport and superconducting properties using maximally localized wannier functions, *Comput. Phys. Commun.* **209**, 116 (2016).
- [33] N. Marzari, A. A. Mostofi, J. R. Yates, I. Souza, and D. Vanderbilt, Maximally localized wannier functions: Theory and applications, *Rev. Mod. Phys.* **84**, 1419 (2012).
- [34] A. A. Mostofi, J. R. Yates, G. Pizzi, Y.-S. Lee, I. Souza, D. Vanderbilt, and N. Marzari, An updated version of wannier90: A tool for obtaining maximally-localised Wannier functions, *Comput. Phys. Commun.* **185**, 2309 (2014).
- [35] See Supplemental Material for details.
- [36] M. Shishkin and G. Kresse, Implementation and performance of the frequency-dependent GW method within the PAW framework, *Phys. Rev. B* **74**, 035101 (2006).
- [37] M. Shishkin and G. Kresse, Self-consistent GW calculations for semiconductors and insulators, *Phys. Rev. B* **75**, 235102 (2007).
- [38] M. Kaltak, *Merging GW with DMFT*, Ph.D. thesis, University of Vienna, 2015.
- [39] G. Kresse and D. Joubert, From ultrasoft pseudopotentials to the projector augmented-wave method, *Phys. Rev. B* **59**, 1758 (1999).
- [40] P. Pavone, K. Karch, O. Schütt, D. Strauch, W. Windl, P. Giannozzi, and S. Baroni, Ab initio lattice dynamics of diamond, *Phys. Rev. B* **48**, 3156 (1993).
- [41] P. B. Allen and B. Mitrović, *Theory of Superconducting T_c*, Solid State Physics, Vol. 37 (Academic Press, 1983).
- [42] P. B. Allen and R. C. Dynes, Transition temperature of strong-coupled superconductors reanalyzed, *Phys. Rev. B* **12**, 905 (1975).
- [43] M. Graf and P. Vogl, Electromagnetic fields and dielectric response in empirical tight-binding theory, *Phys. Rev. B* **51**, 4940 (1995).
- [44] T. Miyake and F. Aryasetiawan, Screened coulomb interaction in the maximally localized wannier basis, *Phys. Rev. B* **77**, 085122 (2008).
- [45] F. Marsiglio, Eliashberg theory: A short review, *Annals of Physics* **417**, 168102 (2020), Eliashberg theory at 60: Strong-coupling superconductivity and beyond.
- [46] V. V. Tolmachev, Logarithmic criterion for superconductivity, *Dokl. Akad. Nauk SSSR* **140**, 563 (1961).
- [47] P. Morel and P. W. Anderson, Calculation of the superconducting state parameters with retarded electron-phonon interaction, *Phys. Rev.* **125**, 1263 (1962).

- [48] F. Marsiglio and J. Carbotte, Electron – Phonon Superconductivity, in *The Physics of Conventional and Unconventional Superconductors*, edited by K. Bennemann and J. Ketterson (Springer-Verlag, Heidelberg, 2001) pp. 73–162.
- [49] N. Dubrovinskaia, L. Dubrovinsky, W. A. Crichton, E. Zarechnaya, E. I. Isaev, and I. A. Abrikosov, Compressibility of boron-doped diamond, *High Press. Res.* **26**, 79 (2006).
- [50] E. Y. Zarechnaya, E. I. Isaev, S. I. Simak, Y. K. Vekilov, L. S. Dubrovinsky, N. A. Dubrovinskaia, and I. A. Abrikosov, Ground-state properties of boron-doped diamond, *J. Exp. Theor. Phys.* **106**, 781 (2008).
- [51] A. V. Lugovskoi, M. I. Katsnelson, and A. N. Rudenko, Electron-phonon properties, structural stability, and superconductivity of doped antimonene, *Phys. Rev. B* **99**, 064513 (2019).
- [52] A. V. Lugovskoi, M. I. Katsnelson, and A. N. Rudenko, Strong electron-phonon coupling and its influence on the transport and optical properties of hole-doped single-layer inSe, *Phys. Rev. Lett.* **123**, 176401 (2019).
- [53] E. R. Margine and F. Giustino, Anisotropic Migdal-Eliashberg theory using Wannier functions, *Phys. Rev. B* **87**, 024505 (2013).
- [54] S. B. Zhang and J. E. Northrup, Chemical potential dependence of defect formation energies in GaAs: Application to Ga self-diffusion, *Phys. Rev. Lett.* **67**, 2339 (1991).

Supplemental Material

Macroscopic dielectric function of undoped C_3N_4

Figure S1 shows real and imaginary part of the macroscopic dielectric function $\varepsilon_{\mathbf{q}=0}(\omega)$ calculated for undoped C_3N_4 in the independent particle approximation. The dielectric function is used to determine the lowest plasmon frequency from the condition $\text{Re}[\varepsilon_{\mathbf{q}=0}(\omega_{\text{pl}})] = 0$. From Fig. S1, we obtain $\omega_{\text{pl}} \approx 13.9$ eV.

Isotropic Eliashberg equations

Here, we provide an expression for the the Eliashberg equations on the imaginary axis written in the isotropic formulation [53] used in these work to estimate temperature dependence of the the superconducting gap.

$$Z(i\omega_n) = 1 + \frac{\pi T}{\omega_n} \sum_{n'} \frac{\omega_{n'}}{\sqrt{\omega_n^2 + \Delta^2(i\omega_n)}} \lambda(n - n') \quad (\text{S1})$$

$$Z(i\omega_n) \Delta(i\omega_n) = \pi T \sum_{n'} \frac{\Delta(i\omega_{n'})}{\sqrt{\omega_n^2 + \Delta^2(i\omega_n)}} [\lambda(n - n') - \mu_C^*], \quad (\text{S2})$$

where

$$\lambda(n - n') = \int_0^\infty d\omega \frac{2\omega\alpha^2 F(\omega)}{(\omega_n - \omega_{n'})^2 + \omega^2}. \quad (\text{S3})$$

In the equations above, $i\omega_n = i(2n+1)\pi T$ is the fermionic Matsubara frequency, and the summation in Eqs. (S1) and (S2) is running up to the cutoff frequency determined as $\omega_{\text{ph}} = 5\omega_{\text{ph}}^{\text{max}}$ with $\omega_{\text{ph}}^{\text{max}}$ being the maximum phonon frequency.

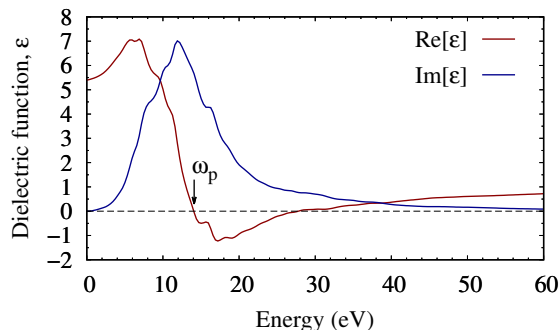


FIG. S1. Real and imaginary part of the macroscopic dielectric function calculated for undoped C_3N_4 in the independent particle approximation. The arrow shows the lowest plasmon energy.

TABLE I. Formation energies E_f (in eV) of boron dopants in C_3N_4 calculated for three different supercells, corresponding to the concentration of 2, 3, and 6 B atoms per nm^3 . The values are given for the substitution of C and N atoms in the C-rich and C-poor conditions.

Concentration	C substitution		N substitution	
	C-rich	C-poor	C-rich	C-poor
$2 \times \text{B} / \text{nm}^3$	-2.41	-1.14	+0.49	-0.46
$3 \times \text{B} / \text{nm}^3$	-2.42	-1.15	+0.51	-0.45
$6 \times \text{B} / \text{nm}^3$	-1.85	-0.58	+0.57	-0.38

Formation energies of B dopants in C_3N_4

The formation energy of boron dopants in C_3N_4 can be calculated as [54]

$$E_f = E_D - E_P + \mu_{C/N} - \mu_B, \quad (\text{S4})$$

where E_D is the energy of a defective relaxed supercell with a boron dopant, E_P is the energy of a supercell without defects. $\mu_{C/N}$ is the chemical potential of a replaced C or N atom, and μ_B is the chemical potential of the B dopant. In Eq. (S4), we do not explicitly consider the charge transfer term because here we only deal with a small hole doping induced by B. Indeed, the maximum possible charge transfer induced by B in the highest considered concentration ($6 \times \text{B} / \text{nm}^3$) is $0.25 |e|$, meaning a marginal contribution to the formation energy.

In this work, we assume that B atoms can substitute either C or N atoms in C_3N_4 , and calculate the formation energies of these two processes. To this end, we use three different supercells, corresponding to the concentration of 6, 3, and 2 B atoms per nm^3 . Specifically, we employ $(1 \times 2 \times 2)$, $(2 \times 2 \times 2)$, and $(2 \times 2 \times 3)$ supercells with the compositions $C_{11}BN_{16}$, $C_{23}BN_{32}$, $C_{35}BN_{48}$ for the C \rightarrow B substitution, and $C_{12}BN_{15}$, $C_{24}BN_{31}$, $C_{36}BN_{47}$ for the N \rightarrow B substitution. The chemical potentials μ_C and μ_N in Eq. (S4) are dependent on the formation conditions. In our calculations, we consider C-rich and C-poor conditions. In the former case, we take $\mu_C = \mu_C^{\text{bulk}}$, where μ_C^{bulk} is the chemical potential of C atoms in diamond. In this case, μ_N is determined from the condition

$$\mu_{C_3N_4} = 3\mu_C + 4\mu_N, \quad (\text{S5})$$

where $\mu_{C_3N_4}$ is the energy of pristine C_3N_4 per formula unit. In the C-poor case, $\mu_N = \mu_N^{\text{bulk}}$, where μ^{bulk} is the chemical potential of N atoms in the α phase of crystalline nitrogen. Similarly, μ_C is determined from the condition given above. In all cases, we take $\mu_B = \mu_B^{\text{bulk}}$, where μ_B^{bulk} is the chemical of B atoms in the α phase of rhombohedral boron. The calculated formation energies are given in Table I.

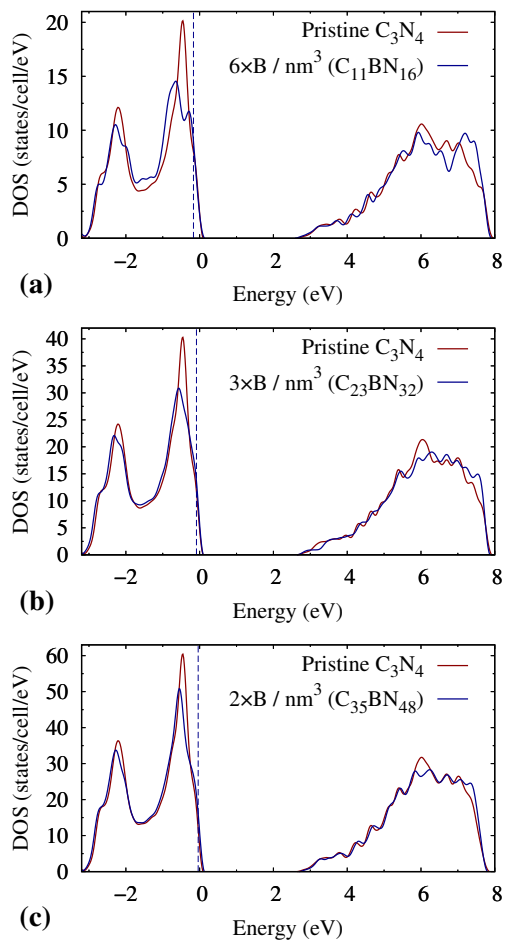


FIG. S2. Electron DOS of boron-doped C_3N_4 calculated for three different supercells, corresponding to the concentration of 2, 3, and 6 B atoms per nm^3 , as well as for pristine C_3N_4 . Zero energy corresponds to the valence band edge. Vertical line is the Fermi energy of the doped system. A shift of the Fermi energy from the valence band edge increases with the B concentration.

Electronic structure of B-doped C_3N_4

The calculations of the formation energies reveal that the substitution of C by B in C_3N_4 is considerably more energetically favorable than the substitution of N. In Fig. S2, we show the electronic DOS for the case of C \rightarrow B substitution compared to the DOS of pristine C_3N_4 . The doping of boron induces a shift of the Fermi energy toward negative energies, which increases with the B concentration. The form of the electronic spectrum remains essentially unchanged in the presence of doping. At the largest considered concentration of $6 \times \text{B} / \text{nm}^3$ one can see a splitting of the main peak, which takes place below the Fermi energy, which is not affecting the states in the immediate vicinity of the Fermi energy.

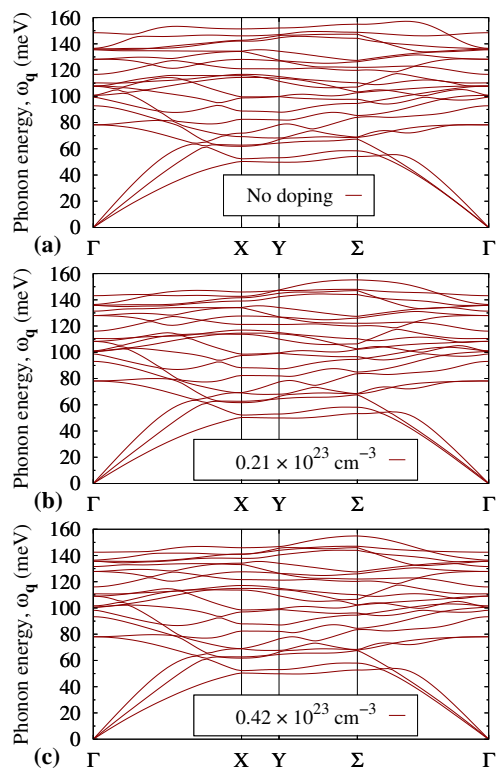


FIG. S3. Phonon dispersion calculated for C_3N_4 under the hole doping induced by adding a positive charge to the system. The dispersion in (a) is calculated without additional charge, whereas (b) and (c) are obtained in the presence of $+0.05$ and $+0.1$ $|e|$ per unit cell, respectively. The absence of imaginary modes indicates dynamical stability of moderately doped C_3N_4 .

Dynamical stability of hole-doped C_3N_4

Figure S3 shows phonon dispersion calculated for C_3N_4 under the hole doping induced by adding a positive charge to the system. The dispersion in Fig. S3(a) is calculated without additional charge, whereas Figs. S3(b) and S3(c) are obtained in the presence of $+0.05$ and $+0.1$ $|e|$ per unit cell, respectively.

Convergence tests

Figures S4(a) and S4(b) show numerical convergence of the averaged Coulomb interaction μ_C and the electron-phonon coupling constant λ with respect to the density of \mathbf{k} and \mathbf{q} meshes. The results presented in the main text for the Coulomb pseudopotential were obtained using $(65 \times 65 \times 65)$ \mathbf{k} -point and \mathbf{q} -point meshes. The electron-phonon coupling was presented for a $(64 \times 64 \times 64)$ \mathbf{k} -point and $(32 \times 32 \times 32)$ \mathbf{q} -point meshes.

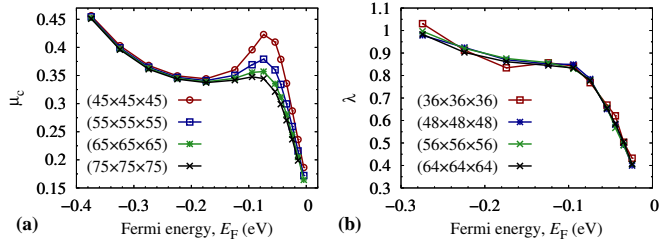


FIG. S4. Numerical convergence of the Brillouin zone integrals with respect to the \mathbf{k} - and \mathbf{q} -point meshes. (a) Coulomb interaction averaged over the Fermi surface μ_C as a function of E_F . (b) Electron-phonon interaction constant as a function of E_F . The mesh given in the legend corresponds to the \mathbf{k} points. An equally dense \mathbf{q} -point mesh was used in the μ_C calculations. For the λ calculations, a halved \mathbf{q} -mesh density was used. A Gaussian smearing of 0.01 eV was used in all cases.